Skew-scattering-induced giant antidamping spin-orbit torques: Collinear and out-of-plane Edelstein effects at two-dimensional material/ferromagnet interfaces

Frederico Sousa,[1] Gen Tatara,[2] and Aires Ferreira[1,*]

[1]*Department of Physics, University of York, YO10 5DD York, United Kingdom*

[2]*RIKEN Center for Emergent Matter Science (CEMS), 2-1 Hirosawa, Wako, Saitama 351-0198, Japan*

(Received 14 May 2020; revised 19 August 2020; accepted 25 November 2020; published 22 December 2020)

Heavy metal/ferromagnet interfaces feature emergent spin-orbit effects absent in the bulk materials. Because of their inherent strong coupling between spin, charge, and orbital degrees of freedom, such systems provide a platform for technologically sought-after spin-orbit torques (SOTs). However, the microscopic origin of purely interfacial antidamping SOT, especially in the ultimate atomically thin limit, has proven elusive. Here, using two-dimensional (2D) van der Waals materials as a test bed for interfacial phenomena, we address this problem by means of a microscopic framework accounting for band structure effects and impurity scattering on equal footing and nonperturbatively. A number of unconventional and measurable effects are predicted, the most remarkable of which is a giant enhancement of antidamping SOT in the dilute disorder limit induced by a robust skew scattering mechanism, which is operative in realistic interfaces and does not require magnetic impurities. The newly unveiled skew scattering mechanism activates rich semiclassical spin-charge conversion effects that have gone unnoticed in the literature, including a collinear Edelstein effect with nonequilibrium spin polarization aligned with the direction of the applied current.

DOI: 10.1103/PhysRevResearch.2.043401

I. INTRODUCTION

When a current is driven through a surface with broken inversion symmetry, a nonequilibrium spin polarization is induced due the spin-orbital-entangled character of electronic wave functions. If coupled to a ferromagnetic system, the emergent spin polarization transfers angular momentum to local spin moments, changing their state by exerting a torque $\mathbf{T} \propto \mathbf{m} \times \mathbf{S}$ [1–4].

Current-induced spin-orbit torques (SOTs) are conventionally classified into two broad categories depending on their behavior under time reversal $\mathcal{T}$: the $\mathbf{m}$-odd or *fieldlike* SOT that affects the precession around the effective magnetic field and the $\mathbf{m}$-even or *antidamping* torque that renormalizes the Gilbert damping and is responsible for the magnetization switching [5–7]. Thinning down heterointerfaces and devices by utilizing van der Waals (vdW) crystals opens up intriguing possibilities. Fueled by the discovery of ferromagnetism in 2D materials, recent works have reported SOT switching of vdW-bonded ferromagnets (FMs), an important stepping stone toward the all-electrical control of atomically thin spin memories [8–11]. Conversely, nonmagnetic 2D crystals with heavy atomic elements can be used as a *source* of interfacial SOT. Experiments employing WTe_2 [12–14], a transition metal dichalcogenide (TMD) with reduced crystal symmetry, have observed strong out-of-plane antidamping torques, which are relevant for high-density magnetic memory applications. While these findings represent significant steps toward SOT devices based entirely on 2D vdW crystals [15,16], the understanding of the underlying mechanisms remains in its infancy.

In this article, we identify and quantify the dominant scattering-dependent mechanisms of SOT generation for a wide class of weakly disordered 2D vdW monolayers and their typical heterostructures. To this end, we develop a microscopic framework wherein all interfacial spin-dependent interactions experienced by charge carriers (including magnetic exchange interaction in arbitrary direction) are treated nonperturbatively, which gives access to the full SOT angular dependence so far inaccessible by rigorous diagrammatic treatments. An exact resummation scheme of single-impurity diagrams is found to capture a unique interplay between spin and lattice-pseudospin degrees of freedom that activates *all* SOT components compatible with hexagonal symmetry [17], i.e., $\mathbf{T} = t_{o1}(\phi)\mathbf{m} \times (\hat{z} \times \mathbf{J}) + t_{e1}(\phi)\mathbf{m} \times [\mathbf{m} \times (\hat{z} \times \mathbf{J})] + t_{o2}(\phi)\mathbf{m} \times (\mathbf{m} \times \hat{z})(\mathbf{m} \cdot \mathbf{J}) + t_{e2}(\phi)\mathbf{m} \times \hat{z}(\mathbf{m} \cdot \mathbf{J})$, with $\hat{z}$ the versor normal to the 2D plane, $\phi = \arccos(\mathbf{m} \cdot \hat{z})$, $\mathbf{J}$ the current density, and $t_{e(o)i}$ with $i = 1, 2$ the torque efficiencies. This unusual proliferation of SOTs that *scale linearly with the interface 2D conductivity* stems from skew-scattering-induced nonequilibrium spin polarization with components along *all* spatial directions. Surprisingly, as shown below, the $\mathbf{m}$-even torques acquire significant magnitudes already for graphene-based heterostructures with C_{6v} symmetry. These technologically relevant SOTs are highly sensitive to the impurity potential strength as well as proximity effects that

*aires.ferreira@york.ac.uk

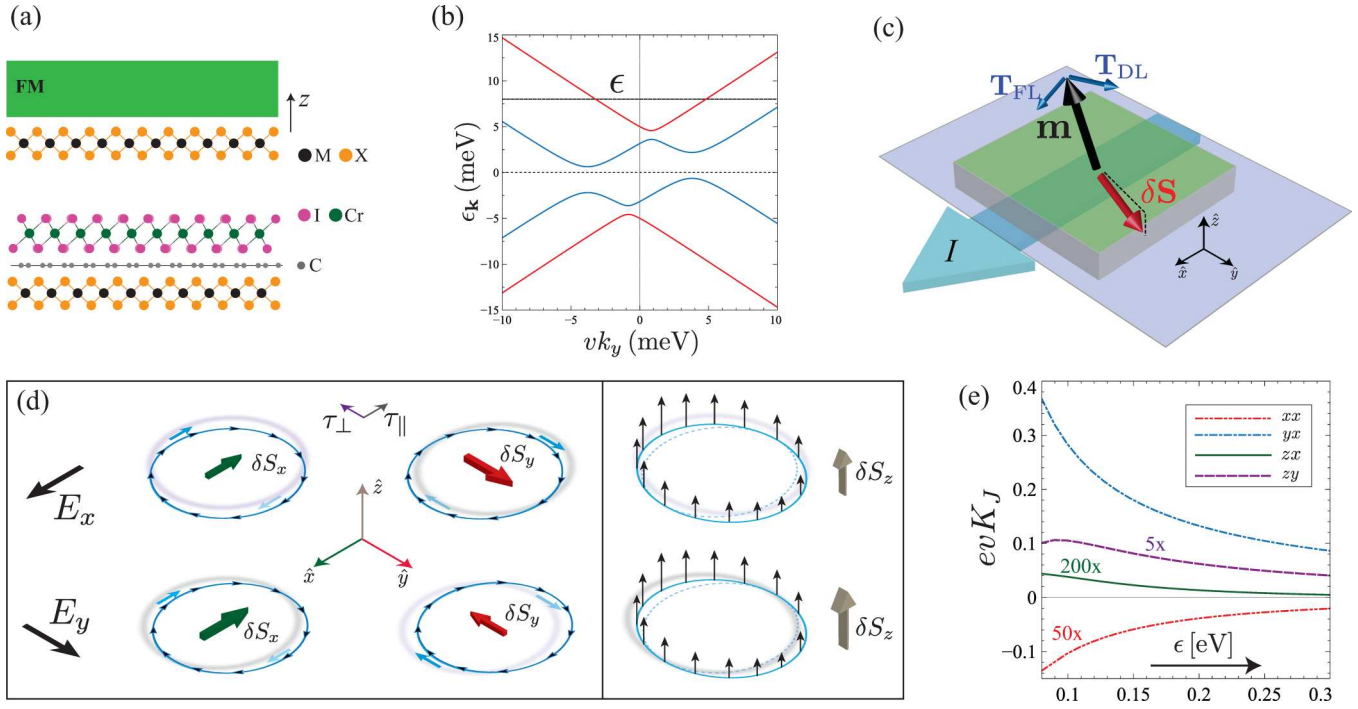

FIG. 1. (a) Schematic of a TMD/thin-film-FM (top) and TMD/graphene/2D-FM bilayer (bottom). (b) Electronic structure around K points in reference heterostructure (plotted along a path with $k_x = 0$). (c) Geometry of 2D material SOT-operated device. Direction of SOTs is indicated for current applied along positive $\hat{x}$ axis assuming $\epsilon > 0$. (d) Current-induced distortion of the Fermi surface in the relaxation-time approximation (gray) and full distortion accounting for skew scattering events, $\delta f_{\mathbf{k}} \propto \tau_\parallel \hat{\mathbf{k}} \cdot \mathbf{E} + \tau_\perp (\hat{\mathbf{k}} \times \mathbf{E}) \cdot \hat{z}$ (purple). 3D arrows depict the net nonequilibrium spin polarization density. (e) Fermi energy dependence of SOT efficiencies for reference C_{6v}-invariant monolayer system. Parameters: $\lambda = 20$ meV, $\Delta_{\mathrm{xc}} = 15$ meV, $\phi = \pi/11$, $n = 10^{11}$ cm^{-2}, and $u_0 = 1.2$ eV nm^2.

reduce the point group symmetry. This is encouraging as local symmetry breaking and disorder landscape can be engineered with nanofabrication methods.

II. MODEL

The low-energy excitations in vdW heterostructures made of typical monolayer compounds, such as graphene and TMDs [see Figs. 1(a) and (b)], are governed by the following generalized Dirac-Rashba model, where $\xi = \pm$ signs refer to valleys $K(+)$ and $K'(-)$:

$$\mathcal{H}_\xi = \int d\mathbf{x}\, \psi_\xi^\dagger \big[v\, \boldsymbol{\Sigma} \cdot (-\imath \boldsymbol{\nabla} + \boldsymbol{\mathcal{A}}_\xi) + \xi \Delta \Sigma_z + \mathcal{A}_\xi^0 - \epsilon \big] \psi_\xi ; \tag{1}$$

$(\psi_\xi, \psi_\xi^\dagger) \equiv (\psi_\xi(\mathbf{x}), \psi_\xi^\dagger(\mathbf{x}))$ are 4-component spinor fields defined on the internal spaces of sublattice (Σ) and spin (s), $v \simeq 10^6$ m/s is the bare Fermi velocity of 2D Dirac fermions, and ϵ is the Fermi energy [18–23]. The gauge-field components $\mathcal{A}_\xi^\mu$ ($\mu = 0, x, y, z$) in the Hamiltonian (1) are 2×2 matrices of the form $\mathcal{A}_\xi^\mu = \sum_{a=x,y,z} \mathcal{A}_{\xi a}^\mu s_a$, which account for all possible spin-dependent effects [24]. The Pauli matrices Σ^a and s^a ($a = x, y, z$) all anticommute with $\mathcal{T}$, so that their products are invariant under time reversal (which also interchanges valleys $\xi \leftrightarrow -\xi$). The staggered on-site potential (Δ) describes orbital-gap opening due to broken sublattice symmetry [25,26]. The ubiquitous interfacial Bychkov-Rashba (BR) effect, with coupling strength λ, is captured by the gauge-field components $\mathcal{A}_{\xi y}^x = -\mathcal{A}_{\xi x}^y = \lambda/v$ [27,28]. Other spin-orbit effects include intrinsic spin-orbit coupling (SOC) of McClure-Yafet-Kane-Mele type ($\mathcal{A}_\xi^z = \lambda_0 s_z$) and spin-valley coupling ($\mathcal{A}_\xi^0 = \xi \lambda_{\mathrm{sv}} s_z$) [29], which plays a crucial role in spin relaxation [30–33] and spin Hall effect [22].

The interaction between the spin of 2D carriers and the local moments in the adjacent FM layer induces an interfacial exchange field, $\mathcal{A}_\xi^0 = -\Delta_{\mathrm{xc}} \mathbf{m} \cdot \mathbf{s}$, with $\Delta_{\mathrm{xc}} > 0$. A nonzero in-plane exchange coupling ($m_{x,y}$) lifts the rotational symmetry of the effective Hamiltonian (1), which will entail the coexistence of in-plane and out-of-plane nonequilibrium spin polarization (more on this later). Representative energy bands for a reference graphene/FM heterostructure are shown in Fig. 1(b). Without loss of generality, we choose the in-plane exchange coupling along the $\mathbf{x}$ axis and write $\mathbf{m} = m_x \hat{x} + m_z \hat{z} \equiv \sin\phi \hat{x} + \cos\phi \hat{z}$ [Fig. 1(c)]. Thus, our microscopic theory encompasses both perpendicularly and in-plane magnetized SOT devices. The lowest carrier density regime in Fig. 1(b) exists only in the anisotropic case ($m_x \neq 0$) and exhibits an electron ($\epsilon > 0$) or hole ($\epsilon < 0$) pocket away from the K point. At intermediate carrier densities, we find a "Mexican-hat" dispersion, followed by a narrow spin-gap region with a single (distorted) Fermi ring [34]. At high electronic density, the two spin-split bands with counterrotating spin textures are occupied. The spin texture of spin-majority states [colored blue in Fig. 1(b)], as well as the current-induced distortion of the Fermi surface, are illustrated in Fig. 1(d). The out-of-plane component of the spin texture can be triggered by an exchange field, spin-valley coupling, or

competition between BR and orbital effects (see below and Appendix A for more details).

III. MICROSCOPIC THEORY OF EXTRINSIC SOT

A. Semiclassical picture

We first determine the interfacial SOTs activated by impurity scattering mechanisms using a semiclassical analysis; then we derive a general microscopic picture for current-induced spin polarization in 2D vdW heterostructures and discuss its consequences. For the first part, we restrict the discussion to C_{6v}-invariant models, which already display the essential phenomenology. A general symmetry-based analysis of the spin-charge response function is given in Appendix B. The first step is to determine the spin texture at the Fermi energy. Perturbation theory in the anisotropy parameter yields, after a long but straightforward calculation, $\mathbf{s}_{\mathbf{k}\nu} = \nu(\mathbf{s}^0_{\mathbf{k}} + \delta\mathbf{s}_{\mathbf{k}})$, with the signs $\nu = \pm 1$ for majority/minority-spin bands [marked blue/red in Fig. 1(b)], $\mathbf{s}^0_{\mathbf{k}} = \varrho_\parallel \hat{k} \times \hat{z} + m_z \varrho_\perp \hat{z}$ the noncoplanar spin texture induced by an out-of-plane exchange combined with BR effect, and $\delta\mathbf{s}_{\mathbf{k}} = (\gamma_\parallel + \mu_\parallel)\,\mathbf{m} \cdot \hat{k} + 2\mu_\parallel \hat{k} \times (\hat{k} \times \mathbf{m}) + m_z \mu_\perp \hat{k} \times \mathbf{m}$ the correction induced by m_x, or, in a more intuitive form,

$$\delta\mathbf{s}_{\mathbf{k}} = m_x[\gamma_\parallel \hat{x} + \mu_\parallel(\cos 2\theta\, \hat{x} + \sin 2\theta\, \hat{y}) - m_z \mu_\perp \sin\theta\, \hat{z}], \tag{2}$$

with θ the wave vector angle. In these expressions, all the coefficients $\{\varrho_{\parallel(\perp)},\ \gamma_\parallel,\ \mu_{\parallel(\perp)}\}$ are functions of $k = |\mathbf{k}|$, λ, and m_z^2. The spin-helical component (in $\mathbf{s}^0_{\mathbf{k}}$) yields the well-known inverse spin-galvanic effect ($\mathbf{S} \propto \varrho_\parallel \hat{z} \times \mathbf{J}$), which is ubiquitous in heterointerfaces [23,35–39]. This nonequilibrium spin polarization exerts a fieldlike torque $\mathbf{T}_{o1} \propto \mathbf{m} \times (\hat{z} \times \mathbf{J})$. Concurrently, the m_x-induced distortion to the spin texture [Eq. (2)] produces *out-of-plane* spin polarization $S_z \propto m_x m_z J_y$, when a current is applied transverse to the in-plane anisotropy axis [see Fig. 1(d)]. This generates a fieldlike SOT that is sensitive to the direction of the applied current, $\mathbf{T}_{o2} \propto \mathbf{m} \times (\mathbf{m} \times \hat{z})(\mathbf{m} \cdot \mathbf{J})$. This newly unveiled effect, which can be traced back to the unique Dirac-Rashba character of electronic states, still occurs when the two spin-split bands (with opposite-in-sign $\hat{z}$ polarizations) are populated. This avoided cancellation of nonequilibrium out-of-plane spin polarization stems from the interplay of pseudospin and spin angular momentum, which renders contributions from spin-split bands inequivalent. This differs from 2D electron gases, for which the only robust SOT is $\mathbf{T}_{o1}$ [7].

To explain the emergence of robust antidamping SOTs, we add the effect of a finite transverse scattering time to the picture. Semiclassically, the nonequilibrium spin polarization is obtained as $\mathbf{S} = \sum_{\mathbf{k}\nu} \mathbf{s}_{\mathbf{k}\nu} \delta f_{\mathbf{k}\nu}$, where $\delta f_{\mathbf{k}\nu} \propto \tau^\nu_\parallel \hat{k} \cdot \mathbf{E} + \tau^\nu_\perp (\hat{k} \times \mathbf{E})_z$ is the deviation of the distribution function away from equilibrium [40]. Consider an electric field applied along $\hat{\mathbf{x}}$. The Fermi surface is shifted perpendicular to the applied current by an amount $\delta f^\perp_{\mathbf{k}\nu} \propto (\tau^\nu_\perp \sin\theta) E_x$. This results in an extrinsic anomalous Hall effect [34], but it also provides an efficient mechanism for current-induced collinear spin polarization S_x as shown here. Skew scattering plays an essential role as there must be an imbalance between scattering cross sections at angles $\pm\theta$, relative to $\mathbf{E}$; otherwise all the states in the Fermi surface will have their S_x component canceled by states with opposite angle. This mechanism is operative under rather general conditions because the spin-orbit-coupled carriers experience an average out-of-plane Zeeman field $\hat{z} \cdot \langle \mathbf{s}_{\mathbf{k}\nu} \rangle_{\mathrm{FS}} \propto m_z$ that breaks the left/right symmetry of scattering events, regardless of the impurity potential specifics, where $\langle \ldots \rangle_{\mathrm{FS}}$ denotes the average over the Fermi surface. After performing the angular integration accounting for a finite $\tau^\nu_\perp$, we easily find the magnetoelectric effect: $\mathbf{S} \propto m_z \varrho_\parallel \mathbf{E}$. The generation of collinear nonequilibrium spin polarization can be extremely efficient in the clean limit due to its inherent semiclassical scaling $\tau_\perp \propto \tau_\parallel \propto n^{-1}$ (where n is the impurity density) [41]. This phenomenon, which we term the *collinear Edelstein effect,* contributes with an antidamping SOT $\mathbf{T}_{e1} \propto \mathbf{m} \times [\mathbf{m} \times (\hat{z} \times \mathbf{J})]$. From Eq. (2), one can easily conclude that the skewness also activates an out-of-plane spin response, $S^z \propto \tau_\perp m_x m_z E_x \propto m_x m_z^2 E_x$. This yields an additional antidamping torque $\mathbf{T}_{e2} \propto \mathbf{m} \times \hat{z}\,(\mathbf{m} \cdot \mathbf{J})$. These SOTs, which scale favorably with the conductivity $\sigma_0 \propto \epsilon\, \tau_\parallel/\hbar \gg 1$, are our central result. The semiclassical mechanisms are summarized in Fig. 1(d).

B. *T*-matrix diagrammatic approach

To derive an accurate microscopic theory of SOT that includes intrinsic effects and disorder corrections (impurity scattering) self-consistently, we extend the controlled diagrammatic technique developed in Refs. [20–23] to arbitrary multiband models. Our approach has two essential features. First, it is fully nonperturbative in the energy scales of the bare Hamiltonian, which includes orbital mass Δ, exchange field vector, BR interaction λ, and other couplings. This technique allows us to explore rich scenarios, including the experimentally relevant regime of proximitized materials with competing energy scales, e.g., $\lambda \approx \Delta_{\mathrm{xc}} \approx \epsilon$. Simple analytical expressions can be obtained to leading order in m_x by developing the Green's functions in Dyson series [7]. Second, the three-leg spin-charge correlation or vertex function $\Gamma_{i\alpha\beta}(\mathbf{x}, \mathbf{y}, \mathbf{z}) = \langle T\, J_i(\mathbf{x}) \Psi_\alpha(\mathbf{y}) \Psi^\dagger_\beta(\mathbf{z}) \rangle$ is evaluated by resumming *all* single-impurity Feynman diagrams, which provides the dominant contribution to the spin-charge response functions in the dilute impurity regime. This is accomplished by writing a Bethe-Salpeter equation with T-matrix insertions [20], which is more general and accurate than the standard approach based on ladder diagrams [Figs. 2(a) and 2(b)]. This allows us to obtain virtually exact results in the dilute regime as well as to explore the crossover between the standard weak Gaussian limit and the important unitary scattering regime, which physically corresponds to resonant scattering from vacancies or adatoms [42,43].

We are interested in SOTs generated by weakly disordered 2D materials and thus focus our subsequent analysis on Fermi surface processes. The latter are captured by the spin density–charge current response function [20,44]

$$K_{ai} = \frac{1}{2\pi} \mathrm{Tr}[s_a \langle G^+ J_i G^- \rangle], \tag{3}$$

with $G^\pm$ the retarded (+)/advanced (−) Green's function, $J_i = -e\,\partial_{p_i} \mathcal{H}_{\mathbf{p}} = -ev\Sigma_i$ the charge current operator, and Tr the trace over all degrees of freedom. Here the angular brackets denote disorder averaging and $\mathcal{H}_{\mathbf{p}}$ is the extension of the

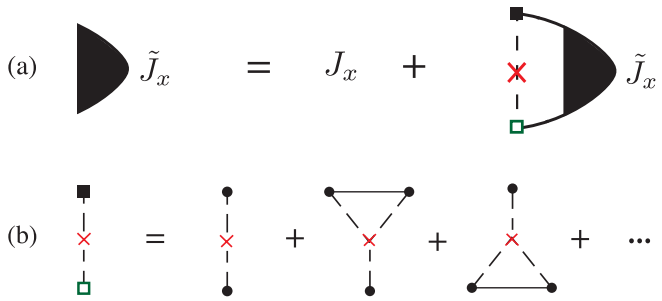

FIG. 2. Diagrammatic expansion of the response function. (a) Bethe-Salpeter equation for the charge current vertex in the *R-A* sector. (b) Skeleton expansion of the T-matrix ladder. Full (open) square denotes a T ($T^\dagger$) matrix insertion, while circles represent electron-impurity interaction vertices. The red $\times$ stands for impurity density insertion (n).

single-particle Hamiltonian to the space of two valleys. Since our aim is to develop a generic SOT theory, which does not rely on the existence of spinful scattering centers, such as spin-orbit-active impurities [45–49], we assume a standard scalar short-range potential $V(\mathbf{x}) = u_0 \sum_{i=1}^{N} \delta(\mathbf{x} - \mathbf{x}_i)$, where $\mathbf{x}_i$ are random impurity locations and u_0 parametrizes the potential scattering strength. Leading terms $K_{ai} \propto 1/n$ in the dilute impurity regime are obtained by replacing in Eq. (3) $\langle G^+ J_i G^- \rangle \to \mathcal{G}^+_{\mathbf{p}} \tilde{J}_i \mathcal{G}^-_{\mathbf{p}}$, where $\mathcal{G}^\pm_{\mathbf{p}}$ is the disorder-averaged Green's function and $\tilde{J}_i$ is the renormalized vertex [Figs. 2(a) and 2(b)]. The final trace in Eq. (3) is carried out using an exact SO(5) decomposition of the response function; technical details will be published elsewhere [50].

IV. RESULTS

A. Graphene-based heterostructures

Armed with this formalism, we evaluate the SOTs and determine their efficiency. Within linear response theory, we write $\mathbf{T} = d^{-1}\, \mathbf{m} \times \mathbf{H}_T$, where d is the FM thin-film thickness, $\mathbf{H}_T = -\Delta_{\rm xc}\, \hat{K}^J \cdot \mathbf{J}$ is the current-induced spin-orbit field, and $\hat{K}^J \equiv \hat{K} \cdot \hat{\sigma}^{-1}$, with $\hat{\sigma}$ the conductivity tensor, is a 3×2 matrix that quantifies the underlying SOC transport effects. The earlier semiclassical picture suggests the decomposition (to leading order in m_x)

$$K^J = \begin{pmatrix} m_z \kappa^{ss}_{\parallel} & \kappa_E \\ -\kappa_E & m_z \kappa^{ss}_{\parallel} \\ m_x \kappa^{ss}_{zx} & m_z m_x \kappa_{zy} \end{pmatrix}, \tag{4}$$

where the superscript ss marks the responses activated by skew scattering. The Fermi energy dependence of K^J for a graphene heterostructure is shown in Fig. 1(e). The highly efficient Edelstein-type response ($\kappa_E \sim 0.4$ for $\epsilon \sim 0.1$ eV) is reminiscent of topological surface states and nonmagnetic graphene/TMD bilayers [23,39]. This process is accompanied by the generation of robust out-of-plane spin polarization. This is at variance with 2D electron gases in Rashba ferromagnets, for which $K^J_{zy} \to 0$ in the weak scattering limit [7]. Concurrently, the newly unveiled skew scattering mechanism, which is operative in all systems with $m_z \neq 0$, enriches the class of SOTs to include $\mathcal{T}$-odd ($\mathbf{m}$-even) terms. Despite the moderate scattering potential strength in Fig. 1(e), a collinear Edelstein response is induced K^J_{ii} ($i = x, y$). The total spin-orbit field thus comprises $\mathbf{H}^{\rm e1}_T \propto \mathbf{m} \times \mathbf{J} \times \hat{z}$ and $\mathbf{H}^{\rm e2}_T \propto \hat{z}\, \mathbf{m} \cdot \mathbf{J}$ antidamping contributions. Owing to its skew scattering origin, the spin-orbit fields scale *linearly* with the conductivity with an efficiency $K^J_{ii} \sim (\sigma_0)^0 \sim n^0$. This behavior is notoriously different from predicted $\mathcal{T}$-odd torques for topological insulators, whose quantum-side-jump origin [21] yields $K^J_{ii} \sim 1/\sigma_0$ in the clean limit [39].

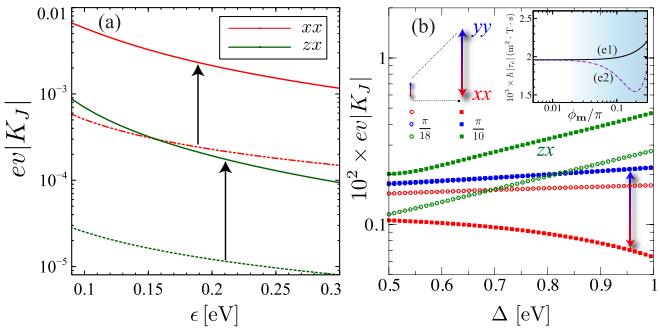

FIG. 3. (a) Giant enhancement of dampinglike SOT due to skew scattering for proximitized graphene. Dashed (solid) lines are calculated in the weak (unitary) scattering regime with $u_0 = 0.1$ eV nm^2 ($u_0 \to \infty$). Other parameters as in Fig. 1(e). (b) Highly anisotropic SOT generated by TMDs in the unitary limit. Orbital-gap dependence of $\mathcal{T}$-odd SOTs is evaluated at fixed carrier density $n_e \simeq 4.7 \times 10^{13}$cm^{-2} for $\phi_{\mathbf{m}} = \pi/10$ (squares) and $\phi_{\mathbf{m}} = \pi/18$ (circles). Inset: Angle dependence of $\tau_{\rm e1(2)}$ for $\Delta = 0.75$ eV. Shaded area indicates nonperturbative region where high-order harmonics in $t_{ei}(\phi)$ become prominent. Other parameters: $\Delta_{\rm xc} = 0.1$ eV, $\lambda = 60$ meV, $\lambda_{\rm sv} = 3$ meV, and impurity density $n = 10^{11}$ cm^{-2}.

An unprecedented sensitivity of the SOT efficiency to the potential scattering strength is borne out by our theory. In contrast to the Edelstein efficiency (κ_E), which receives slow (logarithmic) disorder corrections [23,51], *all dampinglike efficiencies* exhibit a monotonic increase with u_0. This important feature is illustrated in Fig. 3(a), where a tenfold increase in both K^J_{ii} and K^J_{zx} approaching the unitary regime of a resonant scatterer ($u_0 \to \infty$) can be observed. In the weak scattering regime ($u_0 \rho \ll 1$) with $\epsilon \gg \{\lambda, \Delta_{\rm xc}\}$, where ρ is the clean density of states, the leading-order coefficients in the $\mathbf{m}$ expansion of the current-induced torque ($t_{{\rm e(o)}i} \equiv d^{-1} \Delta_{\rm xc} \tau_{{\rm e(o)}i}$) admit a compact analytic form (to leading order in m_x)

$$\tau_{\rm o1} \simeq 2\lambda^3 / f_\epsilon, \quad \tau_{\rm o2} \simeq 2\Delta^2_{\rm xc} \lambda / f_\epsilon, \tag{5}$$

$$\tau_{\rm e1} \simeq u_0 \Delta_{\rm xc} \epsilon\, \lambda^5 / \left(v f^2_\epsilon\right), \quad \tau_{\rm e2} \simeq -\tau_{\rm e1}, \tag{6}$$

where $f_\epsilon = v\epsilon(\lambda^2 + \Delta^2_{\rm xc} m_z^2)$ (see Appendix C). For interpreting these results, it is important to note that the BR coupling should be not too small compared to $k_B T$ so that the torques are appreciable in realistic conditions. Notably, the slow algebraic decay with the Fermi energy $\propto \epsilon^{-1}$ in Eqs. (5) and (6) effectively quenches the effect of thermal fluctuations [23], which in principle allows room-temperature SOT operation even for samples with weak BR effect $\lambda \approx 1$ meV. Recent observations of gate-tunable and reversible spin galvanic effect in graphene-based vdW heterostructures at room temperature

[52–55] provide extra confidence that the interfacial SOTs unveiled here can be demonstrated experimentally.

B. Group-VI dichalcogenides

Next, we consider models with broken sublattice symmetry ($C_{6v} \to C_{3v}$); two examples are shown in Fig. 1(a). As a case study, we focus here on semiconducting TMDs, for which interfacial magnetic exchange coupling can be up to 100 times greater than in graphene-based heterostructures [56–59]. The presence of an orbital gap in TMDs ($E_g = 2\Delta$) modifies the **k**-space spin texture dramatically. We find that the "orbital mass" ($\Delta \gg \lambda$) stabilizes a giant equilibrium out-of-plane spin polarization around K points even in the absence of spin-valley coupling (see Appendix A). To determine the antidamping spin-orbit fields $\mathbf{H}_T^{\mathrm{e1(2)}}$, we evaluate the spin-charge correlation vertex of the full model [Eq. (1)]. Figure 3(b) shows the SOT evolution with the orbital gap. Its most salient feature is a strong enhancement of out-of-plane antidamping efficiency (K_{zx}). This phenomenon is accompanied by a sizable collinear Edelstein effect, with tunable degree of anisotropy $\partial_\Delta |K_{xx} - K_{yy}| > 0$ (e.g., by applying strain), as indicated by the colored arrows. The figure of merit (K^J efficiency) for antidamping SOT generated by electrons in the doped regime ($\epsilon > \Delta$) reaches 4% with $\tau_{\mathrm{e}}/\tau_{\mathrm{o}}$ ratios of order 0.1. A remark is in order. We have thus far employed the commonly used terminology of (anti)dampinglike and fieldlike torques for $t_{\mathrm{e}i}$ and $t_{\mathrm{o}i}$, respectively. Rigorously, one needs to expand these terms in vector spherical harmonics to truly discriminate damping and fieldlike components [60], especially when considering strong in-plane magnetization. In that case $t_{\mathrm{e}i}$ will yield fieldlike contributions and $t_{\mathrm{o}i}$ dampinglike. The leading contributions in the **m** expansion are nonetheless of the nature we have denoted them. (The exceptions are $t_{\mathrm{e}2}$ and $t_{\mathrm{o}2}$ which already at leading order are a mixture of field and damping-like SOTs.) This implies that the presence of K_{zy}, already at the Gaussian level as unveiled here, represents a robust source of genuine dampinglike SOT on its own.

We briefly discuss the implications of our findings for the magnetization dynamics. Crucially, as soon as a finite in-plane magnetization m_x is included nonperturbatively in the microscopic treatment (this is possible only within a numerical approach), the SOT efficiency tensor K_J acquires higher-order harmonics, which invalidates a simplistic analysis in terms of constant "torkances" [Eqs. (5)–(6)] as emphasized recently in Ref. [61]. The shortcoming of the standard approximation can be clearly seen in the TMD-based system, where the SOT becomes highly anisotropic [i.e., $\delta\tau_{12} \equiv ||\tau_{\mathrm{e}2}| - |\tau_{\mathrm{e}1}||/|\tau_{\mathrm{e}1}| \approx 0.25$] for $\phi \approx \pi/10$ [Fig. 3(b)], reflecting the $O(2)$ rotational symmetry breaking. Thus, a fully fledged microscopic treatment for $\mathbf{T}(\phi)$ becomes indispensable to faithfully capture the ensuing magnetization dynamics when solving the Landau-Lifshitz-Gilbert equation [1], irrespective of the FM geometry and its initial macrospin configuration $\mathbf{m}(t = 0)$. The full angular dependence of the torkances is shown in Appendix D for a graphene-based heterostructure. Finally, we emphasize that the angular dependence of the torkances, as well as the leading scaling of antidamping terms $t_{\mathrm{e}1(2)} \propto (\sigma_0)^0$ (resulting in $\mathbf{T}_{\mathrm{e}1(2)} \propto \sigma_0 \propto \tau_\parallel$) reported here, are not captured within perturbative Kubo-Streda calculations for disordered interfaces employed in previous works [7,39,62,63].

V. CONCLUSIONS

In summary, we have reported a microscopic theory of SOT generated by 2D materials proximity coupled to a ferromagnet. The SOTs are evaluated in linear response theory for a generalized Dirac-Rashba model describing 2D vdW heterostructures with C_{6v} or C_{3v} point group symmetry in the presence of smooth magnetic textures, which is readily applicable to SOT devices with both in-plane and perpendicular magnetization. The microscopic calculations are carried out within a T-matrix diagrammatic approach that captures the extrinsic skew scattering contribution to the current-induced SOT inacessible by previous perturbative treatments. We find that skew scattering from non-magnetic impurities enables the robust generation of non-equilibrium non-coplanar spin polarization. Through a complementary semiclassical analysis, we attribute the interfacial skew scattering mechanism to the tilting of the Rashba spin texture caused by the exchange coupling to the ferromagnet. The skewscattering-induced collinear and out-of-plane inverse spin galvanic effects were shown to activate all m-even SOTs compatible with hexagonal symmetry. Interestingly, such m-even SOTs are massively enhanced in the resonant scattering regime of strong impurity potentials (e.g. due to atomically sharp defects), with ratios $|\mathrm{T}|_{\mathrm{even}}/|T|_{\mathrm{odd}}$ on the order of 0.1 for TMD-based heterostructures with large magnetic proximity effect. These semiclassical SOTs scale linearly with the 2D charge conductivity and thus are expected to dominate in the dilute disorder limit. These findings put the spotlight on skew scattering as a promising extrinsic source of technologically relevant antidamping SOTs in weakly disordered interfaces.

ACKNOWLEDGMENTS

A.F. gratefully acknowledges financial support from the Royal Society through a Royal Society University Research Fellowship. We thank K. D. Belashchenko for drawing our attention to the vector spherical harmonic decomposition developed in Ref. [60].

APPENDIX A: ELECTRONIC STRUCTURE AND PSEUDOSPIN-SPIN TEXTURE

The low-energy Hamiltonian of C_{3v}-invariant vdW monolayers reads as

$$H_\xi = \Sigma_\mu (vp + \mathcal{A}_{\mathrm{SO}} + \mathcal{A}_{\mathrm{xc}} + \mathcal{A}_{\mathrm{orb}})^\mu, \tag{A1}$$

where $p^\mu \equiv (-\epsilon/v, p_x, p_y)$ is the 3-momentum of the interface, $\Sigma_\mu = (\Sigma_0, \vec{\Sigma})$, and

$$\mathcal{A}_{\mathrm{SO}} = \lambda\,(s_y\hat{x} - s_x\hat{y}) + \lambda_{\mathrm{KM}} s_z \hat{z} + \xi\lambda_{\mathrm{sv}} s_z \hat{t}, \tag{A2}$$

$$\mathcal{A}_{\mathrm{ex}} + \mathcal{A}_{\mathrm{orb}} = (\mathbf{m}\cdot\mathbf{s})\hat{t} + \xi\,\Delta\,\hat{z}, \tag{A3}$$

are non-Abelian gauge fields capturing all symmetry-allowed SOCs [Eq. (A2)], on-site staggered potential, and interfacial exchange coupling [Eq. (A3)]. Here, $\mathbf{m} = -\Delta_{\mathrm{xc}}\mathbf{m} \equiv \mathfrak{m}(\sin\phi\,\hat{\mathbf{x}} + \cos\phi\,\hat{\mathbf{z}})$ with $\pi \geqslant \phi \geqslant 0$ parametrizes the exchange field. For brevity, in this supplementary information,

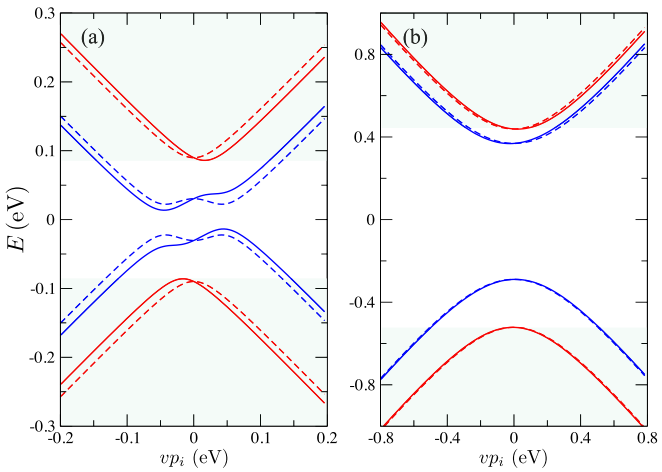

FIG. 4. Electronic structure of a TMD|graphene|FM (a) and TMD|FM (b) heterostructure plotted along $\mathbf{p} = (0, p_y)^t$ (full lines) and $\mathbf{p} = (p_x, 0)^t$ (dashed lines) directions. Shaded areas highlight spectral region II. Parameters: for (a) and (b) $\lambda = 40$ meV, $\mathfrak{m}_x = 20$ meV, $\mathfrak{m}_z = 30$ meV, and for (b) $\Delta = 0.4$ eV, $\lambda_{sv}(\epsilon < 0) = 150$ meV, and $\lambda_{sv}(\epsilon > 0) = 5$ meV.

the analytical expressions are provided for the strong SOC regime with $\lambda > \tilde{\mathfrak{m}}_z \gg \mathfrak{m}_x$ and $\lambda_{KM} = 0$, where $\tilde{\mathfrak{m}}_z \equiv \mathfrak{m}_z + \xi\lambda_{sv}$. Figure 4 shows the low-energy spectrum for two representative systems: (a) TMD/graphene/FM and (b) TMD/FM. In panel (a) only low-energy states (within the TMD gap) are shown. In-plane magnetization ($\mathfrak{m}_x$) breaks the $C_{v\infty}$ symmetry of the continuum model, rending the Fermi surface anisotropic.

The electronic structure comprises four distinct spectral regions:

Regime Ia. Low-energy regime where the Fermi level crosses an electron/hole pocket for

$$\epsilon_{Ia} < |\epsilon| < \epsilon_{Ib}. \tag{A4}$$

Regime Ib. Very narrow energy range where the Fermi level crosses two different Fermi rings both belonging to the spin majority band. This happens for

$$\epsilon_{Ib} < |\epsilon| < \epsilon_{Ic}. \tag{A5}$$

Regime Ic. Intermediate regime where the Fermi level crosses only the spin majority band, hinting at stronger spin density responses for

$$\epsilon_{Ic} < |\epsilon| < \epsilon_{II}. \tag{A6}$$

Regime II. Typical high-electronic-density regime in the experiments. Here, we have $\epsilon > \epsilon_{II}$ and the Fermi level crosses two Fermi rings with opposite spin textures.

The expressions for the different limits are given in Table I. In regime II, the spin operators have the following equilibrium average values at the Fermi energy, in the asymptotic limit $\epsilon \gg \mathfrak{m}_z \equiv \tilde{\mathfrak{m}}_z \gg \mathfrak{m}_x$ (here, θ is the wave vector angle with respect to $\hat{x}$ axis):

$$\langle s_x\rangle \cong \frac{\lambda}{\sqrt{\lambda^2+\mathfrak{m}_z^2}}\left(1-\frac{(\Delta\mathfrak{m}_z+\lambda^2)^2}{2\epsilon^2(\lambda^2+\mathfrak{m}_z^2)}\right)\sin\theta + \frac{\mathfrak{m}_x}{2\sqrt{\lambda^2+\mathfrak{m}_z^2}}\left(1+\frac{\mathfrak{m}_z^2+\lambda^2\cos 2\theta}{\lambda^2+\mathfrak{m}_z^2}\right), \tag{A7}$$

$$\langle s_y\rangle \cong -\frac{\lambda}{\sqrt{\lambda^2+\mathfrak{m}_z^2}}\left(1-\frac{(\Delta\mathfrak{m}_z+\lambda^2)^2}{2\epsilon^2(\lambda^2+\mathfrak{m}_z^2)}\right)\cos\theta + \frac{\mathfrak{m}_x}{2\sqrt{\lambda^2+\mathfrak{m}_z^2}}\frac{\lambda^2\sin 2\theta}{\lambda^2+\mathfrak{m}_z^2}, \tag{A8}$$

$$\langle s_z\rangle \cong \frac{\mathfrak{m}_z}{\sqrt{\lambda^2+\mathfrak{m}_z^2}}\left(1+\frac{\lambda^2}{2\epsilon^2}\frac{\Delta^2-\mathfrak{m}_z^2}{\lambda^2+\mathfrak{m}_z^2}-\frac{\mathfrak{m}_x\lambda\sin\theta}{\lambda^2+\mathfrak{m}_z^2}\right) + \frac{\lambda^4}{\epsilon^2}\frac{\Delta-\mathfrak{m}_z}{(\lambda^2+\mathfrak{m}_z^2)^{3/2}}, \tag{A9}$$

for the spin majority band; the other band has opposite polarity. The pseudospin texture, on the other hand, is

$$\langle\Sigma_x\rangle \cong \left(1-\frac{\lambda^2+\Delta^2}{2\epsilon^2}\right)\cos\theta \pm \frac{\lambda\mathfrak{m}_x}{2\epsilon}\frac{\sin 2\theta}{\sqrt{\lambda^2+\mathfrak{m}_z^2}}, \tag{A10}$$

$$\langle\Sigma_y\rangle \cong \left(1-\frac{\lambda^2+\Delta^2}{2\epsilon^2}\right)\sin\theta \mp \frac{\alpha\mathfrak{m}_x}{2\epsilon}\frac{1+\cos 2\theta}{\sqrt{\lambda^2+\mathfrak{m}_z^2}}, \tag{A11}$$

$$\langle\Sigma_z\rangle \cong \frac{\Delta}{\epsilon} \mp \frac{\mathfrak{m}_z}{\sqrt{\lambda^2+\mathfrak{m}_z^2}}\frac{\Delta\mathfrak{m}_z+\lambda^2}{\epsilon^2}\left(1-\frac{\lambda\mathfrak{m}_x\sin\theta}{\lambda^2+\mathfrak{m}_z^2}\right), \tag{A12}$$

for the spin majority (+)/minority (−) bands. Figure 5 shows the spin and pseudospin profiles along the $\hat{x}$ and $\hat{y}$ directions in momentum space. The orbital mass (Δ) broadens up the **p**-space spin texture dramatically, which boosts the generation of out-of-plane spin polarization in applied current.

TABLE I. Spectral regimes of the C_{3v} model. To ease the notation, all couplings are taken to be positive.

	ϵ_{II}	ϵ_{Ic}	ϵ_{Ib}	ϵ_{Ia}
$\Delta = 0$	$\sqrt{\tilde{\mathfrak{m}}_z^2+4\lambda^2}$	$\tilde{\mathfrak{m}}_z + \frac{\mathfrak{m}_x^2}{2\tilde{\mathfrak{m}}_z}$	$\frac{\tilde{\mathfrak{m}}_z\lambda}{\sqrt{\tilde{\mathfrak{m}}_z^2+\lambda^2}} + \frac{\lambda\mathfrak{m}_x\tilde{\mathfrak{m}}_z\sqrt{2\lambda^2+\tilde{\mathfrak{m}}_z^2}}{(\lambda^2+\tilde{\mathfrak{m}}_z^2)^{3/2}}$	$\frac{\tilde{\mathfrak{m}}_z\lambda}{\sqrt{\tilde{\mathfrak{m}}_z^2+\lambda^2}} - \frac{\lambda\mathfrak{m}_x\tilde{\mathfrak{m}}_z\sqrt{2\lambda^2+\tilde{\mathfrak{m}}_z^2}}{(\lambda^2+\tilde{\mathfrak{m}}_z^2)^{3/2}}$
$\Delta \neq 0$	$\tilde{\mathfrak{m}}_z + \Delta$	$\sqrt{(\Delta-\tilde{\mathfrak{m}}_z)^2+4\lambda^2}$	$\frac{\lambda(\Delta+\tilde{\mathfrak{m}}_z)}{\sqrt{\lambda^2+\tilde{\mathfrak{m}}_z^2}} + \frac{\lambda\mathfrak{m}_x\sqrt{\tilde{\mathfrak{m}}_z(\Delta+\tilde{\mathfrak{m}}_z)(2\lambda^2+\tilde{\mathfrak{m}}_z^2-\Delta\tilde{\mathfrak{m}}_z)}}{(\lambda^2+\tilde{\mathfrak{m}}_z^2)^{3/2}}$	$\frac{\lambda(\Delta+\tilde{\mathfrak{m}}_z)}{\sqrt{\lambda^2+\mathfrak{m}_z^2}} - \frac{\lambda\mathfrak{m}_x\sqrt{\tilde{\mathfrak{m}}_z(\Delta+\tilde{\mathfrak{m}}_z)(2\lambda^2+\tilde{\mathfrak{m}}_z^2-\Delta\tilde{\mathfrak{m}}_z)}}{(\lambda^2+\tilde{\mathfrak{m}}_z^2)^{3/2}}$

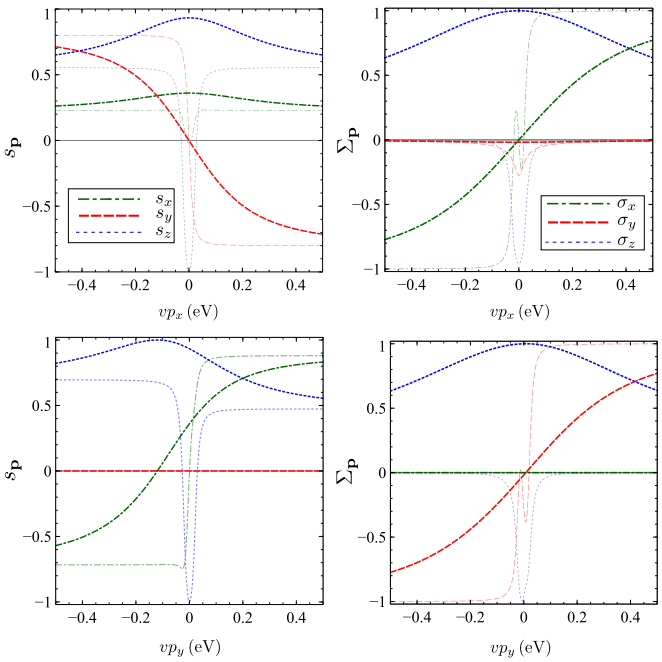

FIG. 5. Emergent pseudospin-spin texture of spin-majority band for a 2D material|FM interface in the presence (thick lines) and absence (thin lines) of orbital gap. The pseudospin-spin textures are plotted along the path $k = (k_x, 0)$ (top panels) and $k = (0, k_y)$ (bottom panels). Band structure parameters: $\lambda = 20$ meV, $\Delta = 400$ meV, $\Delta_{\rm xc} = 15$ meV (with $\phi = \pi/8$), and $\lambda_{\rm sv} = 0$.

APPENDIX B: SYMMETRY ANALYSIS OF FERMI-SURFACE *K*-RESPONSE TENSOR

The Fermi surface density-current response functions are determined from the zero-temperature limit of the term I in the Kubo-Streda formula, namely

$$K_{ai} = \frac{1}{2\pi}\int (d\mathbf{p}) \mathrm{Tr}\{s_a \mathcal{G}^+_{\mathbf{p}} \tilde{J}_i \mathcal{G}^-_{\mathbf{p}}\}, \tag{B1}$$

where $\tilde{J}_i$ is the renormalized current density vertex and $(d\mathbf{p}) \equiv \mathrm{d}\mathbf{p}/(2\pi)^2$. To determine the parity of K_{ai} with respect to the field reversal $\mathfrak{m} \to -\mathfrak{m}$, it suffices to consider the "empty" bubble [7]. The disorder-averaged Green's functions satisfy the following symmetry relations:

$$s_x\sigma_y \mathcal{G}^a(-p_x, p_y)\sigma_y s_x = \mathcal{G}^a(p_x, p_y)|_{S_1}, \tag{B2}$$

$$s_y\sigma_x \mathcal{G}^a(p_x, -p_y)s_y\sigma_x = \mathcal{G}^a(p_x, p_y)|_{S_2}, \tag{B3}$$

$$s_z\sigma_z \mathcal{G}^a(-p_x, -p_y)s_z\sigma_z = \mathcal{G}^a(p_x, p_y)|_{S_3}, \tag{B4}$$

with $S_1 \equiv \{\mathfrak{m}_z \to -\mathfrak{m}_z, \lambda_{\rm sv} \to -\lambda_{\rm sv}, \Delta \to -\Delta\}$, $S_2 \equiv \{\mathfrak{m}_z \to -\mathfrak{m}_z, \mathfrak{m}_x \to -\mathfrak{m}_x, \lambda_{\rm sv} \to -\lambda_{\rm sv}, \Delta \to -\Delta\}$, and $S_3 \equiv \{\mathfrak{m}_x \to -\mathfrak{m}_x\}$. Using these symmetries, we find after some straightforward algebra (sum over repeated indices $a = x, z$ is implied)

$$\{K_{ai}\} = \begin{pmatrix} \mathfrak{m}_z\kappa_{xx} + \mathfrak{m}_a^2\vec{\alpha}_\xi\cdot\vec{f}^a_{xx} + \vec{\alpha}_\xi\cdot\vec{g} & \kappa_{xy} + \mathfrak{m}_z\vec{\alpha}_\xi\cdot\vec{f}_{xy} + \mathfrak{m}_a^2 h^a_{xy} \\ -\kappa_{xy} - \mathfrak{m}_z\vec{\alpha}_\xi\cdot\vec{f}_{xy} + \mathfrak{m}_a^2 h^a_{yx} & \mathfrak{m}_z\kappa_{xx} + \vec{\alpha}_\xi\cdot\vec{g} + \mathfrak{m}_a^2\vec{\alpha}_\xi\cdot\vec{f}^a_{yy} \\ \mathfrak{m}_x\kappa_{zx} + \mathfrak{m}_z\mathfrak{m}_x\vec{\alpha}_\xi\cdot\vec{z}_{zx} & \mathfrak{m}_z\mathfrak{m}_x\kappa_{zy} + \mathfrak{m}_x\vec{\alpha}_\xi\cdot\vec{z}_{zy} \end{pmatrix}, \tag{B5}$$

where $\vec{\alpha}_\xi = \xi(\lambda_{\rm sv}, \Delta)$ and $\{\kappa_{ia}, \mathbf{f}_{ij}, \mathbf{f}^a_{ij}, \mathbf{g}, h^a_{ij}, \mathbf{z}_{zi}\}_{i,j=x,y}$ are even functions of $\mathfrak{m}_x$ and $\mathfrak{m}_z$. The terms linear in $\vec{\alpha}_\xi$ are activated by the breaking of sublattice symmetry, vanishing upon the summation over the two valleys.

APPENDIX C: ANALYTICAL RESULTS FOR WEAK SCATTERING REGIME

For 2D materials with intact sublattice symmetry ($\Delta = \lambda_{\rm sv} = 0$), the self-energy at high carrier density reads as

$$\Sigma^{\pm}(\epsilon) \simeq \mp\imath\eta\left(\mathbf{1} + \frac{\mathfrak{m}_x}{\epsilon}s_x + \frac{\mathfrak{m}_z}{\epsilon}s_z\right), \tag{C1}$$

where $\eta = nu_0^2\epsilon/(4v^2)$ is the disorder-induced quasiparticle broadening. There is already a significant difference at this stage between magnetized Dirac fermions and 2DEGs since, in the latter, the self-energy is a scalar. For 2D Dirac fermions, it is fundamental to keep the full matrix structure of $\Sigma^{\pm}$ in order to obtain physically sensible results that comply with exact symmetry relations of the four-point vertex function, known as Ward identities [22]. In the main text, we presented full nonperturbative results obtained with a numerical inversion of the Bethe-Salpeter equation (Fig. 3). Analytical expressions for the *weak scattering regime* can be obtained by evaluating special subsets of diagrams [20]. Three responses,

TABLE II. Gaussian matrix structures of the renormalized current vertex. In-plane magnetic coupling ($m_x \neq 0$) generates additional orbital-spin mixings, which are fundamental for the accurate description of SOTs.

	$m_x = 0$	$O(m_x)$
$\tilde{J}_x$	$\Sigma_x s_0,\ \Sigma_0 s_y,\ \Sigma_x s_z,\ \Sigma_z s_y$	$\Sigma_x s_x,\ \Sigma_y s_y$
$\tilde{J}_y$	$\Sigma_y s_0,\ \Sigma_0 s_x,\ \Sigma_y s_z,\ \Sigma_z s_x$	$\Sigma_0 s_0,\ \Sigma_z s_0,\ \Sigma_0 s_z,\ \Sigma_x s_y,\ \Sigma_y s_x,\ \Sigma_z s_z$

K_{xy}, K_{yx}, and K_{zy}, are activated at the "Gaussian level" with the standard correlator $\langle V(\mathbf{x})V(\mathbf{x}')\rangle = nu_0^2\delta(\mathbf{x}-\mathbf{x}')$. To capture the antidamping responses K_{xx}, K_{yy}, and K_{zx}, one supplements the ladder series with the Y diagrams generated by the high-order correlator $\langle V(\mathbf{x})V(\mathbf{x}')V(\mathbf{x}'')\rangle = nu_0^3\delta(\mathbf{x}-\mathbf{x}')\delta(\mathbf{x}'-\mathbf{x}'')$. We find for the Gaussian Fermi-surface responses

$$K_{xy} = -K_{yx} = \frac{2}{v\eta}\frac{\lambda^3\epsilon^2\left(\epsilon^2+\mathrm{m}_z^2\right)}{\epsilon^4\left(\lambda^2+\mathrm{m}_z^2\right)-\mathrm{m}_z^4(\epsilon^2-3\lambda^2)}, \tag{C2}$$

$$K_{zy} = -\frac{2}{v\eta}\frac{\lambda \mathrm{m}_x\mathrm{m}_z}{\lambda^2+\mathrm{m}_z^2} + O(\epsilon^{-3}), \tag{C3}$$

$$\sigma_{xx} = \sigma_{yy} = \frac{\epsilon}{\eta}\left(1 - \frac{4\lambda^2\mathrm{m}_z^2(\epsilon^2-2\lambda^2)}{\epsilon^4\left(\lambda^2+\mathrm{m}_z^2\right)-\mathrm{m}_z^4(\epsilon^2-3\lambda^2)}\right), \tag{C4}$$

and

$$K^{\mathrm{Y}}_{xx} = K^{\mathrm{Y}}_{yy} = \frac{u_0\mathrm{m}_z\lambda^5\epsilon^2\left(\epsilon^2-\mathrm{m}_z^2\right)\left(\epsilon^2+\mathrm{m}_z^2\right)^2}{v^3\eta\left[\epsilon^4\left(\mathrm{m}_z^2+\lambda^2\right)-\mathrm{m}_z^4(\epsilon^2-3\lambda^2)\right]^2}, \tag{C5}$$

$$K^{\mathrm{Y}}_{zx} = -\frac{u_0\lambda^5\mathrm{m}_x\mathrm{m}_z^2}{2v^3\eta\left(\lambda^2+\mathrm{m}_z^2\right)^3} + O(\epsilon^{-3}), \tag{C6}$$

$$\sigma^{\mathrm{Y}}_{xy} = -\sigma^{\mathrm{Y}}_{yx} = -\frac{2u_0\mathrm{m}_z\lambda^6\epsilon\left(\epsilon^2+\mathrm{m}_z^2\right)^3}{v^2\eta\left[\epsilon^4\left(\lambda^2+\mathrm{m}_z^2\right)-\mathrm{m}_z^4(\epsilon^2-3\lambda^2)\right]^2}, \tag{C7}$$

for the skew-scattering Fermi-surface terms.

The linear response function at the Gaussian level is determined by a *single* component of the renormalized vertex [51], which provides a transparent scheme to identify candidate nonzero responses K_{ia} based on a symmetry analysis (see Table II). The current vertex transverse to the in-plane magnetic coupling axis ($\tilde{J}_y$) displays a complex structure with a term proportional to s_z, showing that K_{zy} is finite already at the Gaussian level, in agreement with the analysis of Boltzmann transport equations outlined in the main text.

Defining $\gamma_{ij} \equiv \Sigma_i s_j$, one obtains $\tilde{\gamma}_{ij} = \sum_{kl} c_{ijkl}\gamma_{kl}$ with the following nonzero coefficients at the Gaussian level:

$$c_{1010} = c_{2020} = 2 - \frac{4\lambda^2\mathrm{m}_z^2(\epsilon^2-2\lambda^2)}{\epsilon^4\left(\lambda^2+\mathrm{m}_z^2\right)-\mathrm{m}_z^4(\epsilon^2-3\lambda^2)}, \tag{C8}$$

$$c_{1002} = -c_{2001} = -\frac{2\lambda^3\epsilon(\epsilon^2+\mathrm{m}_z^2)}{\epsilon^4\left(\lambda^2+\mathrm{m}_z^2\right)-\mathrm{m}_z^4(\epsilon^2-3\lambda^2)}, \tag{C9}$$

$$c_{2003} = -\frac{2\lambda\mathrm{m}_x\mathrm{m}_z}{\epsilon\left(\lambda^2+\mathrm{m}_z^2\right)} + O(\epsilon^{-2}). \tag{C10}$$

The longitudinal conductivity is determined by Eq. (C8), the Edelstein (inverse spin galvanic) effect is encoded in Eq. (C9), and Eq. (C10) determines the out-of-plane nonequilibrium spin polarization. Replacing the renormalized vertex in the "bubble" [Eq. (B1)] yields the Gaussian response functions presented earlier.

APPENDIX D: FULL ANGULAR DEPENDENCE OF CURRENT-INDUCED SOT

From the knowledge of the spin-charge response tensor $\hat{K}^J(\phi) = \hat{K}(\phi)\cdot\hat{\sigma}(\phi)^{-1}$, one can easily extract the SOT efficiencies or "torkances"

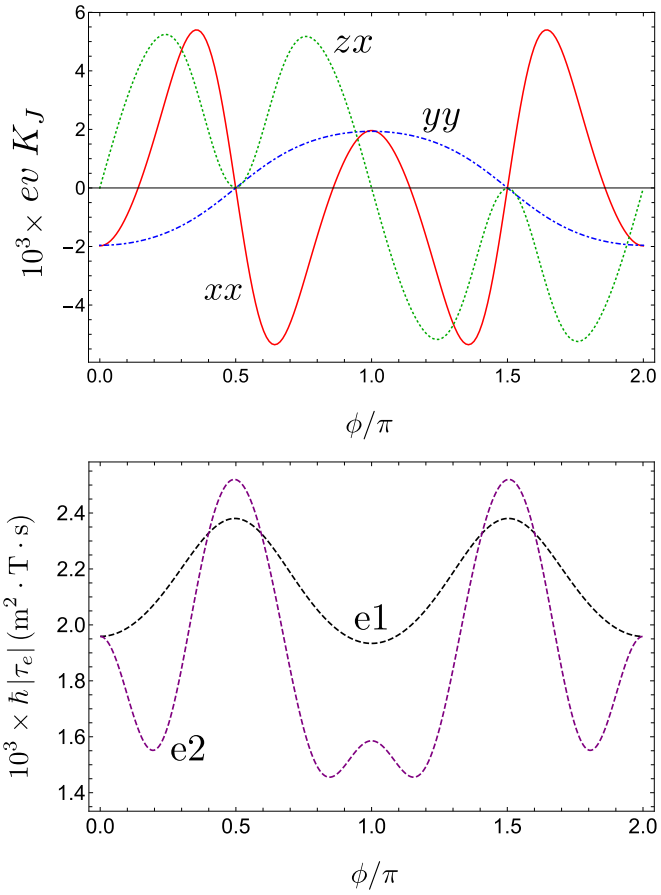

FIG. 6. Angular dependence of **m**-odd response functions (top) and associated SOT efficiencies (bottom). System parameters: $\Delta_{\mathrm{xc}} = 0.1$ eV, $\lambda = 60$ meV, $\lambda_{\mathrm{sv}} = \Delta = 0$, $n = 10^{11}$ cm^{-2}, and $\epsilon = 0.4$ eV.

$$t_{\mathrm{o1}}(\phi) = K^J_{xy}(\phi) - \tan(\phi)\,K^J_{zy}(\phi), \tag{D1}$$

$$t_{\mathrm{o2}}(\phi) = \mathrm{cosec}^2(\phi)\left[K^J_{xy}(\phi)+K^J_{yx}(\phi)\right] - 2\mathrm{cosec}(2\phi)K^J_{zy}(\phi), \tag{D2}$$

$$t_{\mathrm{e1}}(\phi) = \sec(\phi)K^J_{yy}(\phi), \tag{D3}$$

$$t_{\mathrm{e2}}(\phi) = \mathrm{cosec}^2(\phi)\sec(\phi)\left[K^J_{xx}(\phi)-K^J_{yy}(\phi)\right] - \mathrm{cosec}(\phi)K^J_{zx}(\phi) - \sec(\phi)K^J_{xx}(\phi), \tag{D4}$$

entering in the final expression for the current-induced SOT

$$\mathbf{T} = t_{\mathrm{o1}}(\phi)\,\mathbf{m}\times(\hat{z}\times\mathbf{J}) + t_{\mathrm{e1}}(\phi)\,\mathbf{m}\times[\mathbf{m}\times(\hat{z}\times\mathbf{J})] + t_{\mathrm{o2}}(\phi)\,\mathbf{m}\times(\mathbf{m}\times\hat{z})(\mathbf{m}\cdot\mathbf{J}) + t_{\mathrm{e2}}(\phi)\,\mathbf{m}\times\hat{z}\,(\mathbf{m}\cdot\mathbf{J}). \tag{D5}$$

These expressions match those reported by Ado *et al.* [7] (apart from an overall minus sign in the **m**-even torques). The evaluation of the angular dependence of the torkance functions $\{t_{\mathrm{o1}}(\phi), t_{\mathrm{o2}}(\phi), t_{\mathrm{e1}}(\phi), t_{\mathrm{e2}}(\phi)\}$ requires a full nonperturbative treatment beyond previous microscopic formulations [7,39,62,63]. The angular dependence of the skew-scattering-

activated response function and SOT efficiency parameters obtained by a numerically exact procedure is depicted in Fig. 6 for a magnetized graphene layer with strong interfacial exchange and SOC effects.

[1] A. Manchon, J. Zelezny, I. M. Miron, T. Jungwirth, J. Sinova, A. Thiaville, K. Garello, and P. Gambardella, Current-induced spin-orbit torques in ferromagnetic and antiferromagnetic systems, Rev. Mod. Phys. **91**, 035004 (2019).

[2] I. M. Miron *et al.*, Perpendicular switching of a single ferromagnetic layer induced by in-plane current injection, Nature (London) **476**, 189 (2011).

[3] C. O. Avci *et al.*, Current-induced switching in a magnetic insulator, Nat. Mater. **16**, 309 (2017).

[4] S. Shi, Y. Ou, S. V. Aradhya, D. C. Ralph, and R. A. Buhrman, Fast Low-Current Spin-Orbit-Torque Switching of Magnetic Tunnel Junctions through Atomic Modifications of the Free-Layer Interfaces, Phys. Rev. Appl. **9**, 011002 (2018).

[5] T. L. Gilbert, A phenomenological theory of damping in ferromagnetic materials, IEEE Trans. Magn. **40**, 3443 (2004).

[6] K. Garello *et al.*, Symmetry and magnitude of spin-orbit torques in ferromagnetic heterostructures, Nat. Nanotechnol. **8**, 587 (2013).

[7] I. A. Ado, O. A. Tretiakov, and M. Titov, Microscopic theory of spin-orbit torques in two dimensions, Phys. Rev. B **95**, 094401 (2017).

[8] B. Huang *et al.*, Layer-dependent ferromagnetism in a van der Waals crystal down to the monolayer limit, Nature (London) **546**, 270 (2017).

[9] C. Gong *et al.*, Discovery of intrinsic ferromagnetism in two-dimensional van der Waals crystals, Nature (London) **546**, 265 (2017).

[10] M. Alghamdi *et al.*, Highly efficient spin-orbit torque and switching of layered ferromagnet Fe_3GeTe_2, Nano Lett. **19**, 4400 (2019).

[11] X. Wang *et al.*, Current-driven magnetization switching in a van der Waals ferromagnet Fe_3GeTe_2, Sci. Adv. **5**, eaaw8904 (2019).

[12] D. MacNeill *et al.*, Control of spin-orbit torques through crystal symmetry in $WeTe_2$ ferromagnet bilayers, Nat. Phys. **13**, 300 (2017).

[13] D. MacNeill, G. M. Stiehl, M. H. D. Guimaraes, N. D. Reynolds, R. A. Buhrman, and D. C. Ralph, Thickness dependence of spin-orbit torques generated by WTe_2, Phys. Rev. B **96**, 054450 (2017).

[14] S. Shi *et al.*, All-electric magnetization switching and Dzyaloshinskii-Moriya interaction in WTe_2-ferromagnet heterostructures, Nat. Nanotechnol. **14**, 945 (2019).

[15] K. Dolui *et al.*, Proximity spin-orbit torque on a two-dimensional magnet within van der Waals heterostructure: Current-driven antiferromagnet-to-ferromagnet reversible nonequilibrium phase transition in bilayer CrI_3, Nano Lett. **20**, 2288 (2020).

[16] K. Zollner *et al.*, Scattering-induced and highly tunable by gate damping-like spin-orbit torque in graphene doubly proximitized by two-dimensional ferromagnet $Cr_2Ge_2Te_2$ and monolayer WS_2, Phys. Rev. Res. **2**, 043057 (2020).

[17] S. Wimmer, K. Chadova, M. Seemann, D. Ködderitzsch, and H. Ebert, Fully relativistic description of spin-orbit torques by means of linear response theory, Phys. Rev. B **94**, 054415 (2016).

[18] D. Huertas-Hernand, F. Guinea, and A. Brataas, Spin-orbit coupling in curved graphene, fullerenes, nanotubes, and nanotube caps, Phys. Rev. B **74**, 155426 (2006).

[19] D. Kochan, S. Irmer, and J. Fabian, Model spin-orbit coupling Hamiltonians for graphene systems, Phys. Rev. B **95**, 165415 (2017).

[20] M. Milletarì and A. Ferreira, Quantum diagrammatic theory of the extrinsic spin Hall effect in graphene, Phys. Rev. B **94**, 134202 (2016).

[21] M. Milletarì and A. Ferreira, Crossover to the anomalous quantum regime in the extrinsic spin Hall effect of graphene, Phys. Rev. B **94**, 201402(R) (2016).

[22] M. Milletarì, M. Offidani, A. Ferreira, and R. Raimondi, Covariant Conservation Laws and the Spin Hall Effect in Dirac-Rashba Systems, Phys. Rev. Lett. **119**, 246801 (2017).

[23] M. Offidani, M. Milletarì, R. Raimondi, and A. Ferreira, Optimal Charge-to-Spin Conversion in Graphene on Transition-Metal Dichalcogenides, Phys. Rev. Lett. **119**, 196801 (2017).

[24] I. V. Tokatly, Equilibrium Spin Currents: Non-Abelian Gauge Invariance and Color Diamagnetism in Condensed Matter, Phys. Rev. Lett. **101**, 106601 (2008).

[25] Z. Y. Zhu, Y. C. Cheng, and U. Schwingenschlögl, Giant spin-orbit-induced spin splitting in two-dimensional transition-metal dichalcogenide semiconductors, Phys. Rev. B **84**, 153402 (2011).

[26] D. Xiao, G.-B. Liu, W. Feng, X. Xu, and W. Yao, Coupled Spin and Valley Physics in Monolayers of MoS_2 and Other Group-VI Dichalcogenides, Phys. Rev. Lett. **108**, 196802 (2012).

[27] A. Bychkov and E. I. Rashba, Properties of a 2D electron gas with lifted spectral degeneracy, JETP Lett. **39**, 78 (1984).

[28] E. I. Rashba, Graphene with structure-induced spin-orbit coupling: Spin-polarized states, spin zero modes, and quantum Hall effect, Phys. Rev. B **79**, 161409(R) (2009).

[29] C. L. Kane and E. J. Mele, Quantum Spin Hall Effect in Graphene, Phys. Rev. Lett. **95**, 226801 (2005).

[30] A. W. Cummings, J. H. Garcia, J. Fabian, and S. Roche, Giant Spin Lifetime Anisotropy in Graphene Induced by Proximity Effects, Phys. Rev. Lett. **119**, 206601 (2017).

[31] M. Offidani and A. Ferreira, Microscopic theory of spin relaxation anisotropy in graphene with proximity-induced spin-orbit coupling, Phys. Rev. B **98**, 245408 (2018).

[32] T. S. Ghiasi, J. Ingla-Aynes, A. A. Kaverzin, and B. J. van Wees, Large proximity-induced spin lifetime anisotropy in transition-metal dichalcogenide/graphene heterostructures, Nano Lett. **17**, 7528 (2017).

[33] L. A. Benítez *et al.*, Strongly anisotropic spin relaxation in graphene-transition metal dichalcogenide heterostructures at room temperature, Nat. Phys. **14**, 303 (2018).

[34] M. Offidani and A. Ferreira, Anomalous Hall Effect in 2D Dirac Materials, Phys. Rev. Lett. **121**, 126802 (2018).

[35] A. A. Burkov, A. S. Núñez, and A. H. MacDonald, Theory of spin-charge-coupled transport in a two-dimensional electron gas with Rashba spin-orbit interactions, Phys. Rev. B **70**, 155308 (2004).

[36] I. Garate and M. Franz, Inverse Spin-Galvanic Effect in the Interface between a Topological Insulator and a Ferromagnet, Phys. Rev. Lett. **104**, 146802 (2010).

[37] T. Yokoyama, J. Zang, and N. Nagaosa, Theoretical study of the dynamics of magnetization on the topological surface, Phys. Rev. B **81**, 241410(R) (2010).

[38] Ka Shen, G. Vignale, and R. Raimondi, Microscopic Theory of the Inverse Edelstein Effect, Phys. Rev. Lett. **112**, 096601 (2014).

[39] P. B. Ndiaye, C. A. Akosa, M. H. Fischer, A. Vaezi, E.-A. Kim, and A. Manchon, Dirac spin-orbit torques and charge pumping at the surface of topological insulators, Phys. Rev. B **96**, 014408 (2017).

[40] To simplify the analysis, we neglect the θ dependence of the transport times. This is justified since the anisotropy present in the equilibrium spin texture suffices to capture the qualitative behavior of the density-current response function.

[41] This phenomenon is distinct from quantized magnetoelectric effect inside the surface gap of topological insulator/ferromagnet interfaces, $\mathbf{S} = -\sigma_H \mathbf{E}$ with σ_H the Hall conductance, which is a topological effect [36].

[42] Z. H. Ni *et al.*, On resonant scatterers as a factor limiting carrier mobility in graphene, Nano Lett. **10**, 3868 (2010).

[43] A. Ferreira, J. Viana-Gomes, J. Nilsson, E. R. Mucciolo, N. M. R. Peres, and A. H. Castro Neto, Unified description of the dc conductivity of monolayer and bilayer graphene at finite densities based on resonant scatterers, Phys. Rev. B **83**, 165402 (2011).

[44] A. Crépieux and P. Bruno, Theory of the anomalous Hall effect from the Kubo formula and the Dirac equation, Phys. Rev. B **64**, 014416 (2001).

[45] D. A. Pesin and A. H. MacDonald, Quantum kinetic theory of current-induced torques in Rashba ferromagnets, Phys. Rev. B **86**, 014416 (2012).

[46] D. V. Fedorov, M. Gradhand, S. Ostanin, I. V. Maznichenko, A. Ernst, J. Fabian, and I. Mertig, Impact of Electron-Impurity Scattering on the Spin Relaxation Time in Graphene: A First-Principles Study, Phys. Rev. Lett. **110**, 156602 (2013).

[47] A. Ferreira, T. G. Rappoport, M. A. Cazalilla, and A. H. Castro Neto, Extrinsic Spin Hall Effect Induced by Resonant Skew Scattering in Graphene, Phys. Rev. Lett. **112**, 066601 (2014).

[48] A. Pachoud, A. Ferreira, B. Özyilmaz, and A. H. Castro Neto, Scattering theory of spin-orbit active adatoms on graphene, Phys. Rev. B **90**, 035444 (2014).

[49] C. Huang, Y. D. Chong, and M. A. Cazalilla, Direct coupling between charge current and spin polarization by extrinsic mechanisms in graphene, Phys. Rev. B **94**, 085414 (2016).

[50] A. Veneri, F. Sousa, and A. Ferreira (unpublished).

[51] M. Offidani, R. Raimondi, and A. Ferreira, Microscopic linear response theory of spin relaxation and relativistic transport phenomena in graphene, Condens. Matter **3**, 18 (2018).

[52] T. S. Ghiasi, A. A. Kaverzin, P. J. Blah, and B. J. van Wees, Charge-to-spin conversion by the Rashba-Edelstein effect in two-dimensional van der Waals heterostructures up to room temperature, Nano Lett. **19**, 5959 (2019).

[53] L. A. Benítez *et al.*, Tunable room-temperature spin galvanic and spin Hall effects in van der Waals heterostructures, Nat. Mater. **19**, 170 (2020).

[54] L. Lin *et al.*, Gate-tunable reversible Rashba-Edelstein effect in a few-layer graphene/2H-TaS_2 heterostructure at room temperature, ACS Nano **14**, 5251 (2020).

[55] D. Khokhriakov, A. Md. Hoque, B. Karpiak, S. P. Dash, Nature Comm. **11**, 3657 (2020).

[56] J. Qi, X. Li, Q. Niu, and J. Feng, Giant and tunable valley degeneracy splitting in $MoTe_2$, Phys. Rev. B. **92**, 121403(R) (2015).

[57] Q. F. Yao, J. Cai, W. Y. Tong, S. J. Gong, J. Q. Wang, X. Wan, C. G. Duan, and J. H. Chu, Manipulation of the large Rashba spin splitting in polar two-dimensional transition-metal dichalcogenides, Phys. Rev. B **95**, 165401 (2017).

[58] C. Zhao *et al.*, Enhanced valley splitting in monolayer WSe_2 due to magnetic exchange field, Nat. Nanotechnol. **12**, 757 (2017).

[59] T. Norden *et al.*, Giant valley splitting in monolayer WS_2 by magnetic proximity effect, Nat. Commun. **10**, 4163 (2019).

[60] K. D. Belashchenko, A. A. Kovalev, and M. van Schilfgaarde, Interfacial contributions to spin-orbit torque and magnetoresistance in ferromagnet/heavy-metal bilayers, Phys. Rev. B **101**, 020407(R) (2020).

[61] F. Xue, C. Rohmann, J. Li, V. Amin, and P. Haney, Phys. Rev. B **102**, 014401 (2020).

[62] A. Dyrdał and J. Barnaś, Current-induced spin polarization and spin-orbit torque in graphene, Phys. Rev. B **92**, 165404 (2015).

[63] X. Wang and A. Manchon, Diffusive Spin Dynamics in Ferromagnetic Thin Films with a Rashba Interaction, Phys. Rev. Lett. **108**, 117201 (2012).